Materials Today Chemistry 24 (2022) 100990

Contents lists available at ScienceDirect

Materials Today Chemistry

journal homepage: www.journals.elsevier.com/materials-today-chemistry/

A 3D bioelectrical interface to assess colorectal cancer progression *in vitro*

J. Saez [a, b, c, *], A. Dominguez-Alfaro [d], C. Barberio [a], A.M. Withers [a], D. Mecerreyes [c, d], R.M. Owens [a, **]

[a] Department of Chemical Engineering and Biotechnology, University of Cambridge, Philippa Fawcett Drive, Cambridge, CB3 0AS UK
[b] Microfluidics Cluster UPV/EHU, BIOMICs Microfluidics Group, Lascaray Research Center, University of the Basque Country UPV/EHU, Avenida Miguel de Unamuno, 3, 01006, Vitoria-Gasteiz, Spain
[c] Ikerbasque, Basque Foundation for Science, E-48011 Bilbao, Spain
[d] POLYMAT University of the Basque Country UPV/EHU, Joxe Mari Korta Center, Avda. Tolosa 72, 20018 Donostia-san Sebastian, Spain

ARTICLE INFO

Article history:
Received 8 January 2022
Received in revised form
11 May 2022
Accepted 13 May 2022
Available online 17 June 2022

Keywords:
PEDOT
Hyaluronic acid
Collagen
Conductive scaffolds
Electrochemical impedance spectroscopy
Colon cancer
Metastasis

ABSTRACT

Conducting polymers such as PEDOT have attracted considerable attention in the tissue engineering field to add an active electrical read-out to 3D cell cultures. However, PEDOT is normally copolymerized with PSS^- that possibly degrades acidic by-products in the long-term. Given this drawback, it is preferable to tailor PEDOT:polyelectrolyte dispersions that better meet the morphological and physiological micro-environment of the human tissues. Herein, a novel bioelectrical interface in the shape of a 3D porous scaffold made of the conducting PEDOT/hyaluronic acid (HA) and collagen (COL) is presented. For this purpose, first, the oxidative chemical polymerization of 3,4-ethylenedioxythiophene (EDOT) was carried out in the presence of the biopolymers. Then, porous scaffolds were constructed by freeze-drying the dispersions which allows good control of pore size and morphology, showing unique mechanical properties. Interestingly, these biocompatible, conducting scaffolds successfully support growth of 3D cell cultures of sw480 colon adenocarcinoma cancer cells, achieving good cell attachment and proliferation. When integrated with electrodes, they further allow real-time electrical monitoring of cell growth and proliferation. Upon the addition of the flavonoid morin, cell apoptosis and death were monitored by electrochemical impedance spectroscopy and optical immunostaining., demonstrating the promise of these scaffolds for cancer cell progression modeling. We believe that our findings have demonstrated the great promise of combining PEDOT with biopolymers for cancer cell progression modeling but also will be of interest in broader applications in the fields of biomedicine, wearable electronics, and prospectively applied to clinic.

1. Introduction

Research in cancer fundamentals is critical to understanding and treating different types of cancer. Among various types of cancer, colorectal cancer is the third most commonly diagnosed cancer after lung and breast cancer [1]. In the European Union (EU) alone, the annual number of deaths due to colorectal cancer is projected to reach almost 89,000 in 2021 [2]. Most of these deaths occur with metastasis to other organs when cancer cells migrate from a primary tumor to the blood vessels and lymphatics. Recent studies have shown that the extracellular matrix (ECM) plays a key role in metastatic cancer progression, being critical in promoting resistance and recurrence in the tumor microenvironment [3]. These findings have inspired the development of 3D tissue-engineered constructs resembling the in vivo environment and enable the discovery of efficient targeting therapy drugs to cover the growing needs of the worldwide population [4]. Overall, cancer cells grown in 3D configuration express different morphology, motility, and proliferation capabilities, and exhibit higher resistance to anticancer drugs compared to 2D traditional models [5].

3D cell cultures *in vitro* can be sustained in scaffolds that improve cell attachment and guide cells to specific sites for tissue

* Corresponding author.
** Corresponding author.
E-mail addresses: janire.saez@ehu.eus (J. Saez), rmo37@cam.ac.uk (R.M. Owens).

https://doi.org/10.1016/j.mtchem.2022.100990

development [6]. These scaffolds are made of polymers with physiological and biochemical relevance to the tissue of interest allowing the morphological design of structures with dedicated mechanical and compositional properties. Morphologically speaking, native cell environments like the natural ECM are mimicked by adapting the mechanical aspect of the scaffold. Properties such as porosity and stiffness are crucial to ensure interconnected pore networks that aid diffusion of nutrients and oxygen and promote cell attachment with subsequent scaffold colonization [7]. Physiologically speaking, the use of natural polymers such as collagen (COL) and glycosaminoglycans (GAGs) in the composition of the scaffold could be the way to enhance biocompatibility generate templates that support cell growth in the long-term. Among GAGs, hyaluronic acid (HA) is a negatively charged polysaccharide with carboxylic and sulfate functional groups, shown to influence cells through both biochemical (receptor-mediated) and biophysical (structural and mechanical) mechanisms [8]. Biochemically, HA receptors and intracellular-binding proteins have been identified and linked to intracellular signaling affecting cell adhesion, migration, and proliferation. In the tumor microenvironment, HA is known to promote tumor cell migration or enhance migration activity *in vitro* [9]. As an example, a colon adenocarcinoma cell line (sw480) showed a higher spontaneous migration in the presence of HA [10]. Collectively, these findings suggest that HA contributes to relevant changes in the ECM physical properties which may serve as biophysical cues contributing to cell response and cell migration.

Over the past decade, conducting polymers (CPs) such as poly(3,4-ethylenedioxythiophene) (PEDOT) [11,12], polypyrrole (PPy) [13], and polyaniline (PANI) [14], have emerged in the tissue engineering field to add an electroactive capability to 3D cell culture monitoring. Scaffolds made of the semiconductor PEDOT are particularly interesting to promote cell growth by electrical stimulation in bone, muscle, brain [15]. Many groups have exploited the polymer poly(3,4-ethylenedioxythiophene) doped with polystyrene sulfonate (PSS), as a support for cell growth and differentiation of cells, regardless of the possible release of acidic PSS degradation by-products in the long-term [16]. Given this drawback, it is preferable to tailor PEDOT:polyelectrolyte dispersions that better meet the morphological and physiological microenvironment of the human tissues [17]. A variety of negatively charged biomolecules have been studied as polyelectrolytes such as chondroitin sulfate [18], dextran sulfate [19], xantham gum [20], heparin [21], alginate [22], and HA [23] showing improved cell growth and differentiation comparing to the commercial PEDOT:PSS.

3D porous scaffolds can be fabricated by the freeze-drying technique [24]. This technique consists of a first step where dispersions are frozen at a specific cooling ratio, followed by a second step where ice crystals from the frozen dispersions are sublimed at a certain vacuum pressure for several hours. In this way, 3D porous scaffolds are obtained with morphology and mechanical properties akin to human body tissues [25]. This fabrication method has rarely been used in the case of PEDOT conducting polymers.

In this work we present a 3D interface to assess cancer progression based on electroactive scaffolds made of PEDOT:HA and COL that recapitulate the natural ECM *in vitro*. The porous scaffolds were constructed by the freeze-drying technique and were used to electrically monitor cancer cell progression by Electrochemical Impedance Spectroscopy (EIS). sw480 cells were used as a cancer cell model to study the biochemical and biophysical (migration, proliferation) cell-ECM interaction in the ECM microenvironment. The phytochemical compound morin [26] was used as an anti-proliferative drug to induce the apoptosis of cells and validate the system.

2. Results and DISCUSSION

2.1. Synthesis and characterization of PEDOT:Hyaluronic acid and PEDOT:Hyaluronic acid/collagen aqueous dispersions

The synthetic route of dispersions containing the conducting polymer PEDOT and polysaccharide has been reported previously [23]. In this work, a similar synthetic route was followed for the synthesis of PEDOT:HA and PEDOT:HA/COL aqueous dispersions. The chemical oxidative polymerization process followed to obtain the PEDOT:HA and PEDOT:HA/COL dispersions employed different formulations of the initial components. Thus, three different wt% ratios were initially prepared: 15:85, 50:50, and 85:15 for each dispersion. The dispersions were prepared by polymerizing EDOT monomer in the presence of the polysaccharide sodium hyaluronate dissolved in water at room temperature. The dispersions containing 1, 3, and 5 mL of COL (3 mg/mL) (PEDOT:HA/COL1, PEDOT:HA/COL3, and PEDOT:HA/COL5, respectively) were synthesized by adding COL with the sodium hyaluronate, Fig. 1A. Ammonium persulfate ($(NH_4)_2S_2O_8$) was used as an oxidant in the presence of a catalytic amount of iron (III) chloride ($FeCl_3$) (Fig. S1). The reaction takes place slowly and the initial yellowish viscous solution turns to a greyish less viscous solution within the first 6 h. This phenomenon was observed previously with other PEDOT:polysaccharide dispersions and it is ascribed to the PEDOT chains breaking the strong intramolecular hydrogen bonds of the polysaccharide [20]. The polymerization of EDOT is completed in 72 h acquiring a characteristically dark blue color and a viscosity similar to that of water.

While 50:50 and 15:85 wt% ratios present highly continuous drop-casted film formation, 85:15 wt% films present higher discontinuity within the film structure as shown in the scanning electron microscopy (SEM) pictures (Fig. S2). As a result, just the 15:85 wt% was found to be suitable for further investigation as the one showing better aspect-ratio properties. To simplify, the working aqueous dispersions under study were PEDOT:HA, PEDOT:HA/COL1, PEDOT:HA/COL3, and PEDOT:HA/COL5 in wt% 15:85 ratio.

UV−vis−NIR spectroscopy was performed to observe the PEDOT oxidation state obtained in the presence of two insulators additives, sodium hyaluronate, and COL. The dispersions showed two characteristic PEDOT absorption bands (Fig. 1B). The broad absorption band of PEDOT π-π^* is centered at ~800 nm and the bipolaron band is centered at 1200 nm [20]. These two absorption bands present in the UV−vis−NIR spectra indicate the presence of doped PEDOT chains as cation and di-cation species and are related to the conductivity of the material, confirming that PEDOT:HA dispersions are conducting. The presence of these bands confirms the higher presence of doped chains in this PEDOT:HA dispersion, a sign of high conductivity. However, the dispersions containing COL display a depletion of the bipolaron band, indicating that COL may act as an insulator, reducing conductivity.

This observation is in line with the electrical conductivity measured on drop-casted films prepared onto silicon molds and analyzed by a four-point probe (see Fig. S3). PEDOT:HA films possess a conductivity above 10^{-2} S/cm as reported previously [23], which is similar to PEDOT:PSS films formed without additives like COL. The addition of COL shows a decrease in the conductivity in agreement with the presence of insulating species. The addition of 1 mL of COL (PEDOT:HA/COL1) drops the conductivity values to $8 \cdot 10^{-3}$ S/cm and to $2 \cdot 10^{-3}$ S/cm when COL is used for concentrations higher than 3 mL reaching a plateau in conductivity (PEDOT:HA/COL3 and PEDOT:HA/COL5). Although PEDOT:HA dispersions containing COL were found to be less conducting, they were kept under study due to their promising mechanical and biocompatible

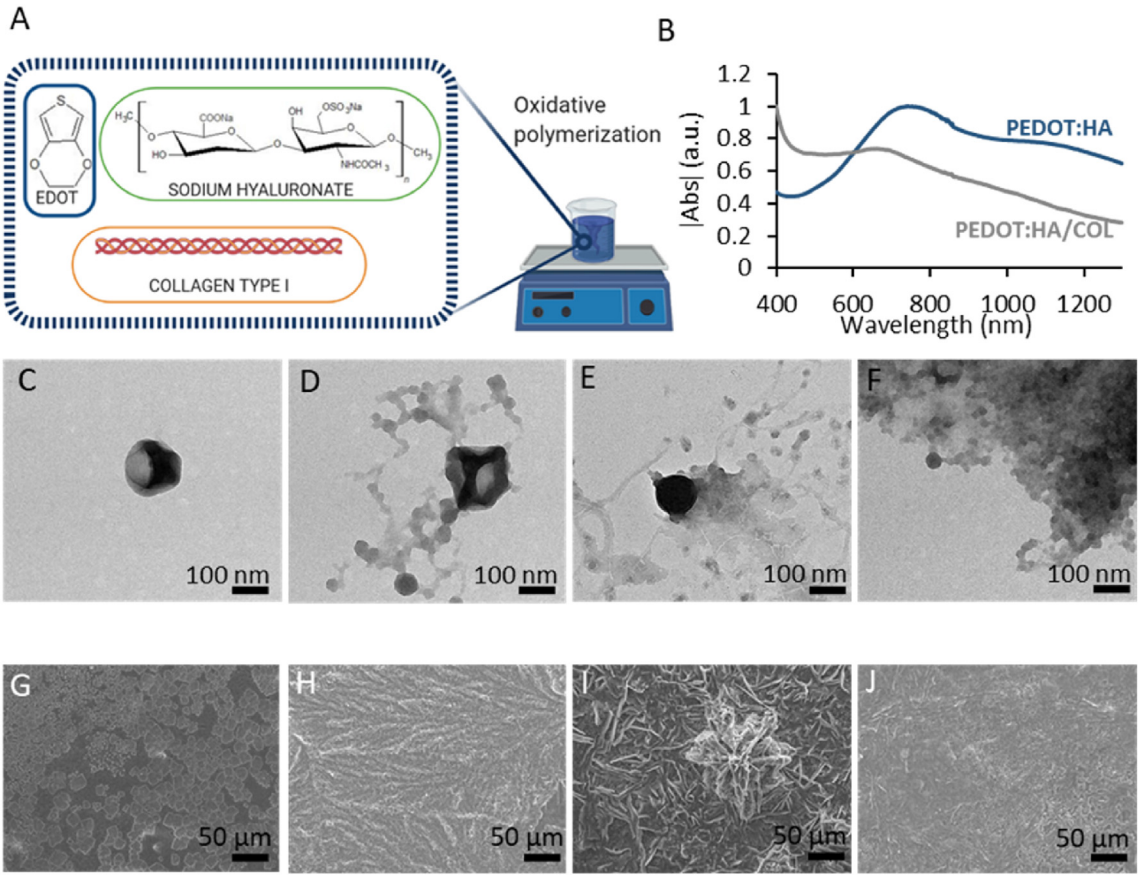

Fig. 1. A) PEDOT:HA and PEDOT:HA/COL synthetic scheme. Inset: cartoon of PEDOT:HA reaction vial at 72 h. B) UV–vis–NIR spectra of PEDOT:HA and PEDOT:HA/COL dispersions showing the higher conductivity for PEDOT:HA in the absence of collagen. C–F) Transmission Scanning Microscopy (TEM) pictures of the dispersions highlighting the collagen networks created around PEDOT:HA particles (in order PEDOT:HA, PEDOT:HA/COL1, PEDOT:HA/COL3, PEDOT:HA/COL5). G-J) Scanning Electron Microscopy (SEM) pictures of the films featuring different surface displays, generally, and increment of collagen creates a smoother surface (in order PEDOT:HA, PEDOT:HA/COL1, PEDOT:HA/COL3, PEDOT:HA/COL5).

properties in recapitulating the physiological microenvironment of the ECM.

The morphology of the PEDOT:HA and PEDOT:HA/COL dispersions was investigated by TEM, Fig. 1C–F. As observed in similar systems [27], the PEDOT:HA dispersions consist of spherical PEDOT particles covered by HA of an average size of 200 nm. In contrast, PEDOT:HA/COL dispersions display a network of interconnected particles with diameters between 600 nm and 1 µm. Interestingly, the addition of COL to the mixture creates a large COL network covering the PEDOT:HA particles, thus, affecting the colloidal morphology (Fig. S4).

Further information on the dispersion properties was obtained via SEM (Fig. 1G–J). Optical analysis was performed on SEM pictures and it was found that PEDOT:HA spherical particles are formed as a result of PEDOT chains being drop-casted, making the spherical particles agglomerate together in the form of a film. PEDOT:HA films present a flower-like structure formed by discontinuous clusters. In contrast, films with increasing concentrations of COL showed a continued and smoother structure, presenting elongated crystals and, as discussed before for TEM, a similar spiderweb-like structure formed by elongated crystals in the PEDOT:HA/COL3 film.

2.2. Preparation and characterization of PEDOT:HA and PEDOT:HA/COL scaffolds

To create a 3D electroactive ECM, porous scaffolds were prepared by the freeze-drying method [25]. The freeze-drying method consists of two parts, Fig. 2A. First, dispersions are frozen down at a set temperature and cooling rate, and second, the ice is sublimed at a set pressure, obtaining porous scaffolds and electrodes for the EIS characterization. In this process, different parameters such as solid content of the dispersion, presence of a crosslinker, and freeze-drying conditions will affect the morphology and mechanical properties of the scaffold. After freeze-drying the different dispersions, the four types of scaffold (Fig. 2B) were analyzed chemically by Fourier transform infrared (FTIR) spectroscopy (Fig. S5) and thermogravimetric analysis (TGA) (Fig. S6). Also, the morphology of the scaffolds was characterized by SEM (Fig. 2C–F). Overall, the scaffolds present an isotropic structure as determined by the ice crystal growth and the solid content. The scaffolds containing COL show a more compact structure due to the higher solid content and two phases separated as the concentration of COL increases (top enriched with COL). We hypothesize that as the ice crystals grow, the polymer chains are pushed aside, concentrating around the growing crystals. Once the ice is removed by sublimation, only a porous skeleton is left where the ice structure was. PEDOT:HA and PEDOT:HA/COL scaffolds show an interconnected porous network that will enhance water and nutrients retention, and cell migration and proliferation. In contrast to PEDOT:HA (pore size 32 ± 6 µm), scaffolds containing COL present a more polydispersed and compact structure featuring slightly smaller pore sizes ranging from PEDOT:HA/COL1 31 ± 2 to PEDOT:HA/COL5 26 ± 5 µm (Fig. S7). In particular, PEDOT:HA/COL3 scaffolds show a spider-web structure (Fig. 2E) that correlates well with the spider-web observed in 2D (Fig. 1I). We envisioned that this porous structure that mimics the ECM would facilitate cell nutrient

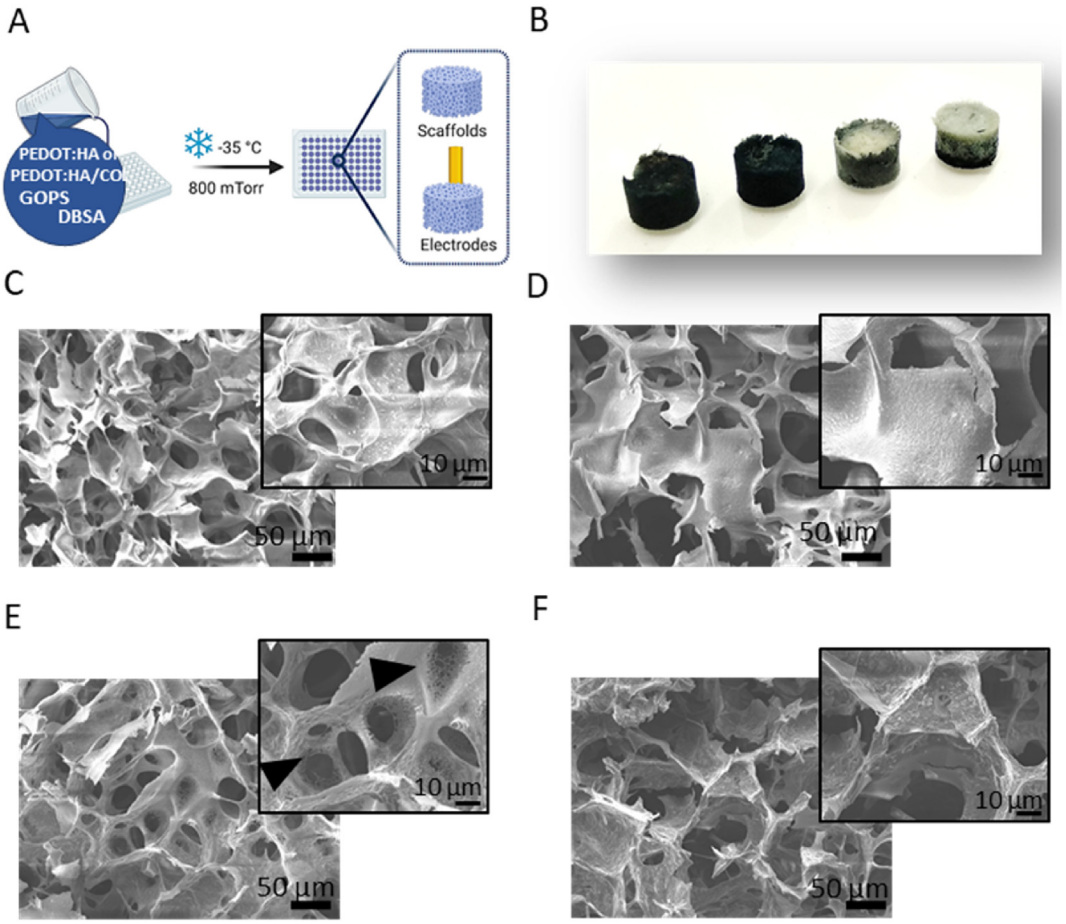

Fig. 2. A) General scheme to manufacture scaffolds. B) Image of the stand-alone scaffolds PEDOT:HA, PEDOT:HA/COL1, PEDOT:HA/COL3, PEDOT:HA/COL5 (left to right). C–F) SEM micrographs showing the pores and structure of the scaffolds. Inset: zoom image of the pores of the scaffold C) PEDOT:HA, D) PEDOT:HA/COL1, E) PEDOT:HA/COL3; black arrows indicate the spider-web structure, F) PEDOT:HA/COL5.

percolation, cell attachment, and colonization [28]. This demonstrates that the addition of increasing concentrations of COL can vary the porosity of the scaffold and its mechanical stiffness.

It is well known that the stiffness of the scaffold affects cell attachment and proliferation [29] and load transfer to the attached cells when the scaffold deforms under physiological conditions. PEDOT:HA and PEDOT:HA/COL mechanical properties were thus investigated. Differences among the mechanical properties of the different scaffolds were evaluated by compression testing. The compression test was performed in dry scaffolds showing Young's modulus values between PEDOT:HA/COL5 20 ± 7 kPa and PEDOT:HA 156 ± 12 kPa (Fig. 3A). As a general trend, the higher the COL content, the higher the Young's modulus of the scaffolds. While it is difficult to compare the scaffolds since they have different pore sizes and contents, the measurements suggest that the scaffolds containing increasing amounts of COL present less stiffness comparing to PEDOT:HA. While increasing the COL content presumably reduces the stiffness of the cell wall material, the increment in PEDOT:HA/COL5 scaffolds noticed in the Young's modulus is probably offset by the two phase separated displayed for the PEDOT:HA/COL5 scaffolds. It is important to mention that the scaffolds were observed to maintain good structural integrity throughout the 7 days in cell culture media, confirming scaffold stability under physiological conditions.

The swelling capacity of scaffolds is linked to porosity and hydrophilicity, being the last key for transferring cell nutrients and cellular metabolites [30]. As explained above, the scaffolds containing COL present a more compact and less porous structure compared to PEDOT:HA scaffolds, likely due to the greater solid content. The scaffolds understudy presented a higher swelling capacity in the absence of COL after 24 h in PBS (pH = 7.4) as shown in Fig. 3B. In contrast, the PEDOT:HA/COL scaffolds were observed to be more hydrophilic when increasing the COL content (visual observation) showing a faster speed of wetting in PBS. PEDOT:HA/COL3 scaffolds exhibited both a decent swelling ratio (SR) and good hydrophilicity.

EIS measurements were run to analyze the effect of the increasing concentration of COL on the overall electrochemical properties of the scaffold. As anticipated, the inclusion of COL is found to be associated with an increase in the material impedance over the mid-low frequency range, as shown in the Bode plot (|Z| *vs* Frequency) in Fig. 3C. This effect is more significant in PEDOT:HA/COL5. To be highlighted is the exhibition of the ohmic flat curve for the scaffolds in the absence or presence of COL [24,25]. The apparent changes were accompanied by the presence of a broad peak in the phase spectrum and an increase in the phase angle maximum with COL content (from 34° to 38°, PEDOT:HA and PEDOT:HA/COL5, respectively), Fig. 3D. Overall, the COL-containing scaffolds were found to keep their conducting characteristics, holding a great promise for using these structures in cell migration and proliferation electrical monitoring.

The presence of HA within the scaffolds was assessed by immunostaining using a biotinylated HA-binding protein (HABP)

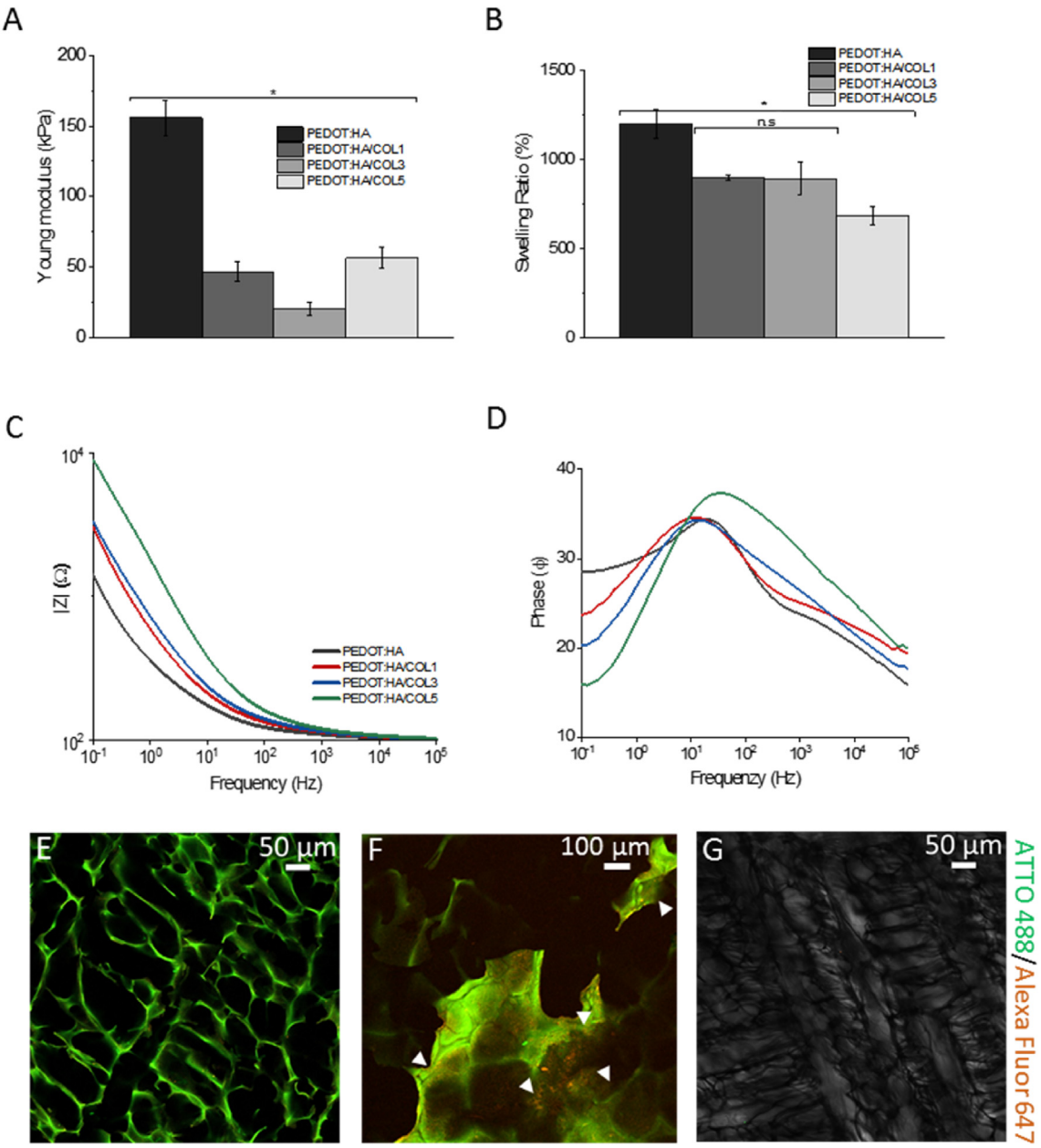

Fig. 3. A) Young's modulus of dry scaffolds (n = 3). PEDOT:HA/COL5 presents a higher Young's modulus due to the two distinct regions of the scaffold (top part collagen concentrated and bottom part PEDOT:HA concentrated) ANOVA *p ≤ 0.05. B) Swelling ratio (%) of PEDOT:HA and PEDOT:HA/COL scaffolds (n = 3) ANOVA *p ≤ 0.05. C-D) Comparative EIS measurements of the different scaffolds showing the C) Bode plot of PEDOT:HA and PEDOT:HA/COL scaffolds, and. D) phase angle vs frequency of PEDOT:HA and PEDOT:HA/COL scaffolds. E) HA (green) immunostaining of PEDOT:HA scaffold, F) HA (green) and collagen (orange, as indicated by white arrow heads) immunostaining of PEDOT:HA/COL3 scaffold and G) Bright field image of PEDOT:PSS scaffold.

method. Biotin was non-covalently bonded to streptavidin-FITC conjugate with high affinity to detect HA in the structure of the scaffold (ATTO488). Moreover, the presence of COL was detected by using a COL type I antibody that binds specifically, using Alexa Fluor 647 as the secondary antibody. As shown in Fig. 3E–F, HA (green) was localized within the whole structure of the PEDOT:HA and PEDOT:HA/COL scaffolds. In contrast, COL presence in PEDOT:HA/COL scaffolds was found to be more localized in the form of clusters as depicted in Fig. 3F and Fig. S8. Non-containing HA and COL PEDOT:PSS scaffolds were used as controls without showing any similar trace or cluster within the structure (Fig. 3G).

2.3. PEDOT:HA and PEDOT:HA/COL scaffolds promote cell proliferation

Given that both HA and COL are ECM-derived constituents, an enhanced cytocompatibility over other similar materials such as PEDOT:PSS is expected. To evaluate cell proliferation on the different scaffolds, an XTT cell viability assay was carried out to quantify metabolic activity of sw480 cancer cells seeded in scaffold slices of 500 µm thickness for 7 days (Fig. 4A). Interestingly, PEDOT:HA showed similar metabolic activity and indirectly cytocompatibility to the control (pristine PEDOT:PSS). In contrast,

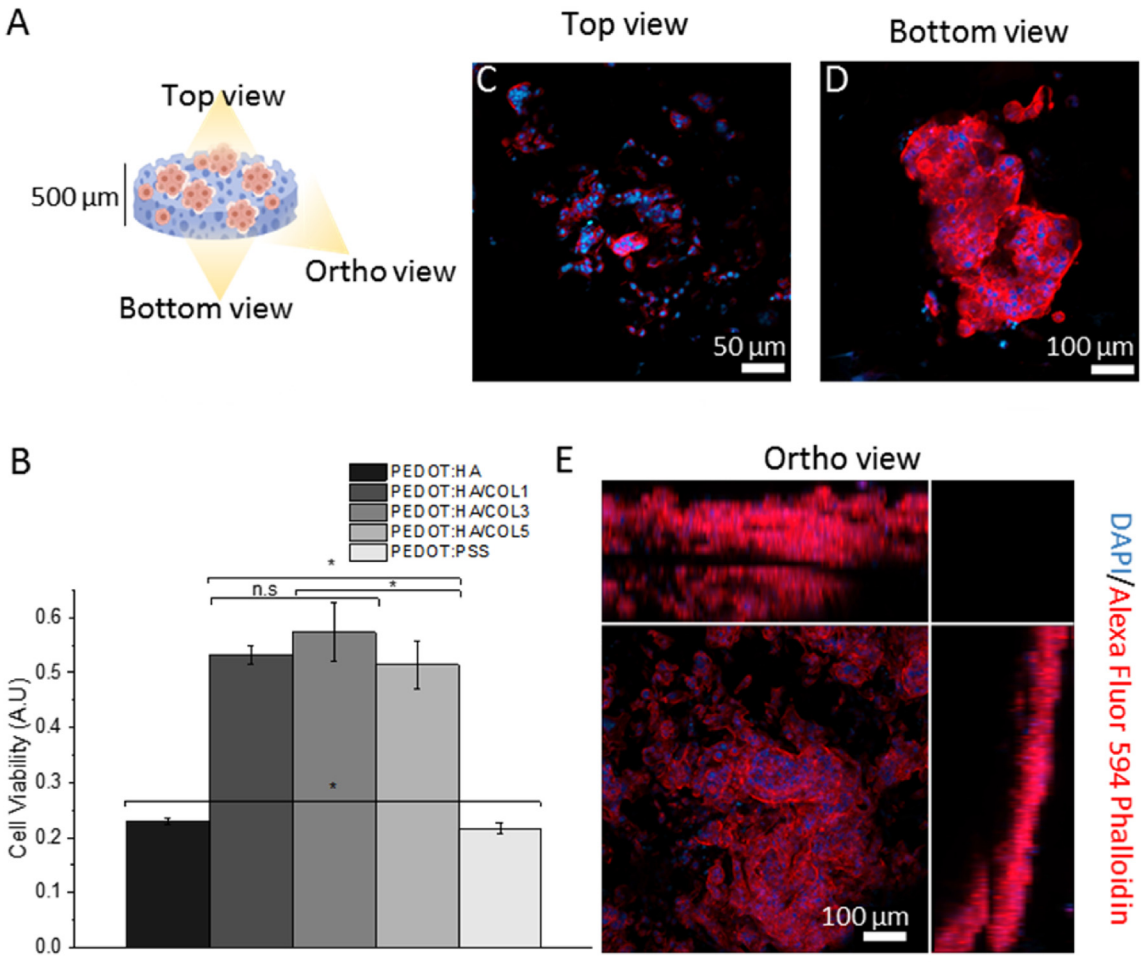

Fig. 4. A) Scheme of a 500 µm scaffold slice seeded with sw480s. B) Viability of sw480 cells measured by XTT assay (n = 3). Absorbance at 450 nm of the 4 samples compared to PEDOT:PSS control. Absorbance values obtained after 7 days of cell culture with an initial seeding cell density of 4×10^4 ANOVA *$p \leq 0.05$. C) Top view, D) Bottom view and E) ortho view of confocal microscopy images showing the nuclei stained with DAPI (blue) and F-actin cytoskeleton stained with Alexa Fluor 594. The ortho view shows the invasiveness of the sw480s through the scaffold (270 µm depth).

scaffolds containing COL showed improved cell survival and proliferation compared to both PEDOT:HA and PEDOT:PSS scaffolds. Of note is the higher cell viability and cell growth observed for PEDOT:HA/COL3 scaffolds (Fig. 4B). From this point, just PEDOT:HA/COL3 scaffolds were considered for developing the electroactive ECM biointerface.

After 7 days of culture, sw480s cells stained for nuclei with DAPI and cytoskeleton (F-actin) with Alexa Fluor 594 Phalloidin, showed high locomotion and migration to the bottom parts of the scaffold presumably enhance by the presence of HA and COL and the interconnected porous network (Fig. 4C–F). Fig. 4G shows an orthoview where sw480s cells have invaded the bottom parts of the scaffold, displaying high cell attachment and coverage. The Video S1 shows a stack of the immunostained cells seeded onto a 500 µm slice.

Supplementary video related to this article can be found at https://doi.org/10.1016/j.mtchem.2022.100990

2.4. 3D electrical and optical monitoring of sw480s progression

As demonstrated by others before [31], conducting scaffolds are capable of showing changes in their electrochemical properties when cells interact, grow, and colonized the scaffold. In this way, conducting scaffolds can be used to trace cell growth and death employing EIS. Only PEDOT:HA/COL3 scaffold-based electrodes were selected to undergo this study as it was considered to be the optimal condition showing the best biochemical and biophysical properties, as explained above. sw480 cells were seeded on a sterilized scaffold at 2.5×10^5 cells and kept under incubation for 7 days (Fig. 5A). Fresh media changes were made at day 3 and 6. After 7 days of culture, scaffolds maintained good structural integrity and stiffness. A two-electrode configuration was used to take the measurements, using a platinum (Pt) mesh as the counter electrode and the connections being, W–S (scaffold-based electrode), and CE-RE (Pt mesh). Fresh media was used as the electrolyte solution. The impedance data showed in the Bode plot (|Z| vs Frequency), revealed a significant increase in the impedance value of a half order of magnitude (from $|Z| \sim 49$ kΩ to $|Z_{cell}| \sim 100$ kΩ at 10^{-1} Hz) in the case of scaffolds containing cells, in the low-frequency range (10^{-1}-10^2 Hz) (Fig. 5B). In this frequency range, ionic transport dominates, thus indicating that cells have grown and filled the porous of the scaffold acting as a barrier for ions to flow. In the mid to high-frequency range (10^2–10^5 Hz), a discrete increment of the impedance values indicates the presence of lining cells on the walls of the scaffold, hindering ion transport. The Nyquist plot further confirms the effects of cells lining the pores of the scaffold in the high-frequency range (Fig. 5C). The phase data suggests the addition of capacitive elements in the circuit as well as an increase of the phase angle from $\varphi \sim 65°$ to $\varphi_{cells} \sim 71°$, which corresponds to the growth of cells in the pores of the scaffold (Fig. 5D).

After establishing the sw480 growth bioelectronic model, apoptosis of cells was induced by the flavonoid compound morin.

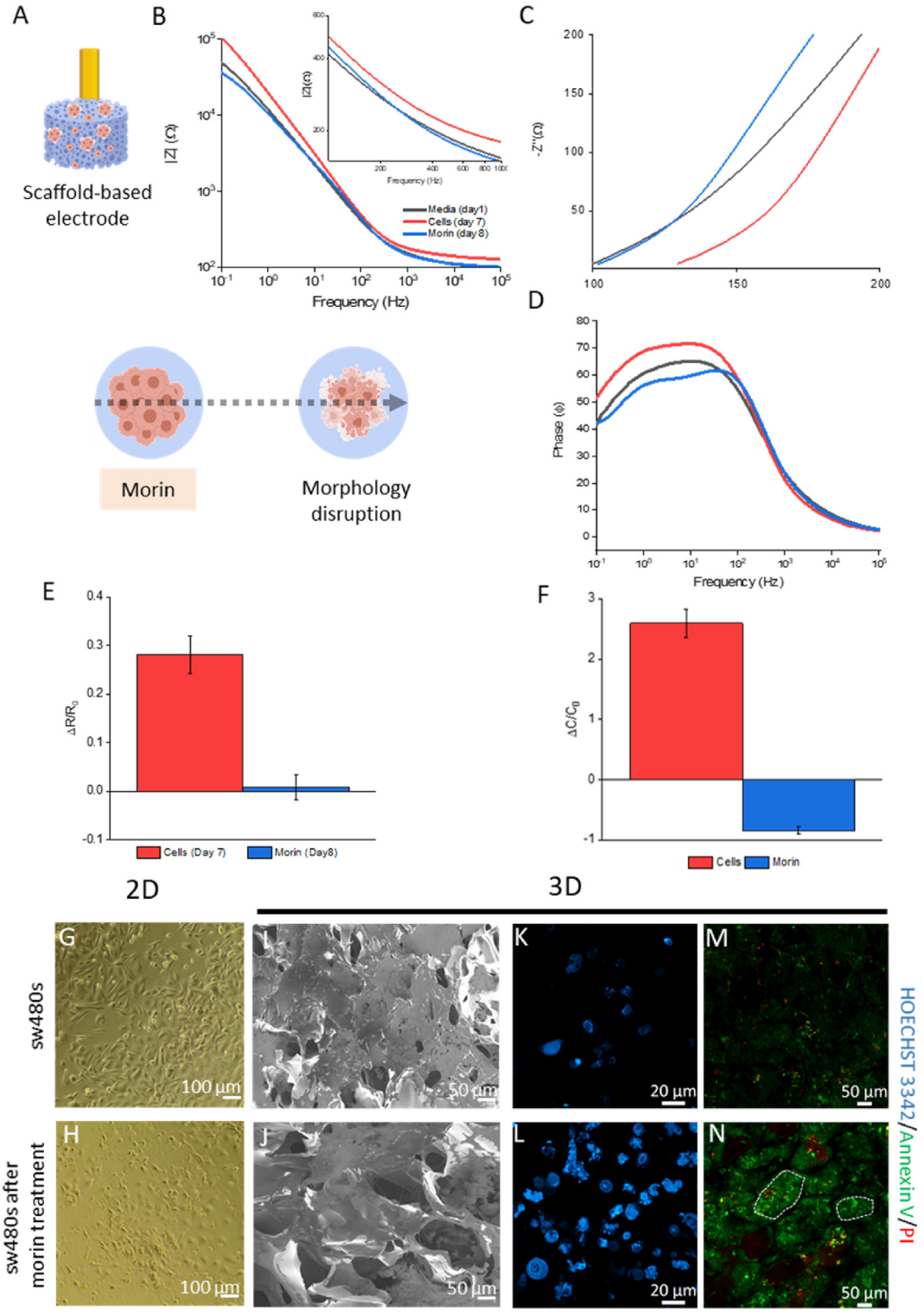

Fig. 5. A) Schematic of a scaffold-based electrode with sw480 cells proliferating. B-G) Impedance study of the adhesion and proliferation of sw480s on the PEDOT:HA/COL scaffold-based electrodes. B-G) Representative B) Bode impedance magnitude C) Nyquist D) Phase plot showing the initial (black line, day 1 before seeding), final (red line, day 7 after seeding), and morin response (blue line, day 8 after morin morphology disruption) of the cultured cells on the electroactive scaffold. Inset in Bode plot shows the evolution of the complex impedance during the tissue formation, from day 1 to day 8 after morin treatment. E-F) Bar plots showing E) the relative change in the resistance ($\Delta R/R_0$), and F) capacitance ($\Delta C/C_0$) of the porous electrodes ($n = 3$) after each stage of seeding. G-H) sw480s microscopy pictures displaying the change of morphology after morin treatment in 2D. I-J) SEM images illustrating cell coverage of the scaffolds before and after morin treatment. K-L) Treated and non-treated scaffolds seeded with sw480s showing DNA damage and chromatin condensation after Hoechst immunostaining. M – N) Confocal microscopy pictures of sw480 cells stained with Annexin-V (FITC) and PI at day 8 with and without morin treatment. White dashes indicate two pores of the scaffold complete filled with cells.

Morin has been previously reported to show anticancer activity and induce apoptosis causing morphology disruption in sw480s cells [32]. 2D experiments of sw480s cells showed a drastic change in the morphology of the cell on morin treatment after 24 h. While untreated control cells showed a smooth surface (Fig. 5H), treatment with morin resulted in severe damage of cells with ostensible deformation, shrunken to abnormal round type and cell number was significantly decreased (Fig. 5I). Electrically, treatment with morin shows a decrease of the impedance values in the low-frequency range to $|Z_{morin}| \sim$ 36 kΩ at 10^{-1} Hz (from $|Z_{cell}| \sim$100 kΩ) indicating cells progression towards death (Fig. 5B). Also, in the high-frequency range (see Bode and Nyquist plots), a decrease of the impedance initial values suggests that cells have detached from the scaffold. This was also confirmed by SEM images of the 3D conducting scaffolds taken before and after morin treatment (Fig. 5I–J). The phase angle also is reduced to $\varphi_{morin} \sim 65°$(from $\varphi_{cells} \sim 71°$) showing a halving phase value attributed to the presence of a disturbing element in the cell culture medium (morin) (Fig. 5D).

Ionic transport opposition due to the presence of growing/apoptotic cells contributes to the increment/decrease of the Relative Resistance ($\Delta R/R_0$) and Relative Capacitance ($\Delta C/C_0$) (Fig. 5F–G) calculated with the corresponding EIS fitting model (Fig. S9) [33]. The resulting EIS model allows monitoring changes in the resistance (from $\Delta R/R_0$ 0.281 ± 0.039 to 0.007 ± 0.026) and capacitance (from $\Delta C/C_0$ 2.590 ± 0.235 to −0.844 ± 0.062) as a result of cell migration and proliferation through the bulk of the scaffold, as well as cell death and loss of connectivity between cells.

The antiproliferative activity shown by morin could be due to the induction of apoptosis and it can be observed by staining the cells with a fluorescent DNA-binding dye. Nuclear alterations like chromatin condensation and DNA fragmentation which are the hallmark of apoptosis were determined by Hoechst 33342 staining. As shown in Fig. 5L, untreated control cells did not show much blue fluorescence, indicating that cells are alive and Hoechst does not easily permeate into the cell nuclei. The fluorescence light was denser and brighter in cells treated with morin along with remarkable nuclear changes of apoptosis such as the formation of apoptotic bodies, condensation of chromatin, and nuclear fragmentation (Fig. 5M). Further confirmation of apoptosis in cells was carried out by staining untreated (Fig. 5N) and morin-treated sw480s (Fig. 5O) with Annexin-V/FITC and propidium iodide (PI). Vital cells are negative for fluorescence-conjugated Annexin-V binding and PI, while early apoptotic cells are positive for Annexin-V but negative for PI, whereas necrotic cells are Annexin-V negative and PI positive. A significant increase in the number of stained apoptotic cells was observed after morin treatment and a slight increase in the number of dead cells (stained for PI), in contrast to untreated cells.

In contrast, controls do not show significant changes in impedance values in the whole frequency range (Fig. S10). The abovementioned findings are consistent with previous studies on similar 3D conducting cell culture systems. A more in-depth study of the electrochemical migration of cells could be done by modifying the scaffold set up and integrating an extra gold electrode in a different part of the scaffold.

3. Conclusions

In this study, novel PEDOT:HA and COL scaffolds with the ability to host and monitor cells are presented. Conducting scaffolds were obtained by synthesizing and freeze-drying PEDOT:HA and PEDOT:HA/COL dispersions through oxidative polymerization. The mechanical properties and porosity of the conducting scaffolds can be tuned with the concentration of the COL and the ratio in between the conducting polymer and polysaccharide, giving the possibility to optimize pore size and stiffness according to the target cell culture. Among all of the scaffolds, PEDOT:HA/COL3 proved its potential to act as a bioelectrical interface to host and monitor sw480 colon adenocarcinoma cancer cells' growth and progression all over the scaffold. By inducing cell apoptosis with morin, optical immunostaining proved that cells lose their morphology and the electrical impedance recovers to initial values. Significantly, this work presents a conducting and biocompatible functional material that provides a powerful tool to better mimic native tissues as well as a platform to monitor electrically small changes produced in cancer cell progression.

4. Experimental section

4.1. Synthesis of PEDOT:HA and PEDOT:HA/COL dispersions

PEDOT:HA and PEDOT:HA/COL dispersion with 2% solid content and at 15:85 ratio were synthesized by oxidative polymerization according to the previous procedure [20]. In a 10 ml vial, 170 mg of sodium hyaluronate was dissolved in 10 mL 9, 7, and 5 mL of Milli-Q water for PEDOT:HA, PEDOT:HA/COL1, PEDOT:HA/COL3, and PEDOT:HA/COL5, respectively. The viscous solution was stirred for 20 min until the HA completely dissolves. Right after, 1 mL, 3 mL, and 5 mL of COL type I from rat tail (3 mg/mL, Gibco) was added respectively (PEDOT:HA/COL1, PEDOT:HA/COL3, and PEDOT:HA/COL5). Afterward, a 1.5 equiv of ammonium persulfate ($(NH4)_2S_2O_8$, Sigma Aldrich) respect to monomer together with a catalytic amount (10 mg) of iron (III) chloride ($FeCl_3$, Sigma Aldrich) was added to the previous aqueous solution. Once the mixture is dissolved, 30 mg of EDOT monomer was added. The reaction was kept at room temperature for 72 h until an intense deep blue color was obtained.

Films of the different dispersions were prepared by drop-casting 200 μL of dispersion in spherical silicon molds of 1 cm diameter. The dispersions were left at room temperature to dry overnight to create a film.

4.1.1. Dispersion characterization

4.1.1.1. UV–Vis characterization. UV–vis–NIR measurements were taken with a UV/vis/NIR Perkin-Elmer lambda 950 spectrometer using quartz cuvettes. 5 v/v % of PEDOT:HA or PEDOT:HA:col solution were dissolve in Milli-Q water and the UV–vis–NIR data was acquired. Spectra were normalized to perform a fair comparison.

4.1.1.2. TEM characterization. TEM images were collected using a JEOL JEM-2100F model EM-20014 (JEOL Ltd, Japan), which features a 200 kV field emission gun (Schottky) "FEG" and an ultra-high-resolution pole piece "UHR." First, 1 μL of the studied sample was solubilized in 1 mL of deionized water to obtain a clear solution. Finally, 5 μL of the solution was deposited onto a copper film TEM grid and evaporated at room temperature.

4.1.1.3. Four-point probe. A four-point probe system (Ossila) was used to evaluate the conductivity of the solid films. PEDOT:HA or PEDOT:HA/COL solutions were drop-casted in spherical glass slides of 12 mm diameter. The films were dried at room temperature.

4.2. Scaffold preparation by freeze-drying method

10 w% PEDOT:PSS (Heraeous PH 1000), 3 wt% of (3-glycidyloxypropyl)trimethoxysilane (GOPS), and 0.5 wt% of dodecylbenzosulfonic acid (DBSA) per mL of dispersion were added to both PEDOT:HA and PEDOT:HA/COL dispersions. Scaffolds were formed by the freeze-drying method with a Virtis Advantage 2.0 Benchtop (SP Scientific). Dispersions were dispersed with 150 μL of each solution in a 96 multi-well plate. The freeze-drying process was

adapted from [24] by changing the temperature to −35 °C with a freezing rate of 0.19 C/min. For the preparation of scaffold-based electrodes, 1.5 cm length, 3 mm width gold-covered Kapton sheets were immersed into each well before freeze-drying. Gold-Kapton was covered with a PDMS solution (1:10 PDMS, curing agent) to prevent secondary short-circuiting. After freeze-drying, the scaffolds were heated up to 49 °C for 4 h to start the crosslinking process. Scaffolds obtained were ~5 mm diameter and ~3 mm height.

Scaffolds not containing gold-Kapton were sliced with a Vibratome (Leica Biosystems) and 500 μm thickness slices were obtained.

4.2.1. Scaffold characterization

4.2.1.1. FTIR and TGA characterization. Infrared spectra were recorded at room temperature with a Thermo scientific model Nicolet is20 FT-IR, Thermo Scientific Inc., USA. The measure was performed on 1 mm slice of the desired scaffold, applying 32 scans in transmission mode.

TGA was performed under air atmosphere (25 mL/min flow rate) using a TGA Discovery (TA Instruments). A piece of 1 mm of the desired scaffold was placed in the Pt pans and inserted in the chamber. First, an equilibration step was set at 100 °C for 20 min. Then, the sample was heated from 100 to 800 °C at a rate of 10 °C/min.

4.2.1.2. SEM characterization. SEM was performed on JEOL JSM-6490LV. PEDOT:HA and PEDOT:HA:col with different COL compositions were sliced in 2.5 mm thickness and mounted on aluminum holder with double-sided carbon tape. The outer and inner shell was evaluated at different magnifications using point-by-point mode.

4.2.1.3. Mechanical characterization. Scaffold pore size was calculated by Image J (Java) analysis. 30 pores of 3 pictures of each scaffold were measured with a ruler and the media was calculated.

Scaffolds were characterized mechanically using Tinius Olsen 5ST (Tinius Olsen Ltd, UK) 1–50 kN. With a Tinius Olsen apparatus, the compressive moduli of the dry scaffolds were calculated. The Tinius Olsen had a load cell of 25 N and the compression speed was set at 1 mm/min. Young's modulus values were calculated from the slope of the linear part of the strain stress curve. Scaffold density was calculated according to their volume and weight.

The water-retaining capacity of the scaffolds was obtained by performing a swelling analysis. Scaffolds were weighed before and after soaking for 24 h in PBS. The SR of the scaffolds was analyzed according to Equation 1.

Equation 1 $L = \frac{W_W - W_D}{W_D} x\ 100$ where.

where, W_W is the weight of the scaffold after soaking with PBS and W_D is the weight of the dry scaffold.

4.2.1.4. Electrical characterization. Scaffolds were characterized by EIS using an Autolab potentiostat (PGSTAT128 N, Metrohm, UK) in the frequency range of 10^{-1} to 10^5 Hz. A two-electrode configuration was set up for the EIS measurements using a commercial platinum mesh as the counter electrode (W–S and RE-CE). The distance between the electrodes was set to ~3 mm. The applied AC voltage was 0.01 V and measurements were carried out at 0 V DC potential *vs* open circuit potential.

4.2.1.5. Scaffold immunofluorescence staining. COL type I and HA immunostaining was performed sequentially. Firstly, 500 μm scaffold slices were blocked with 1% Bovine Serum Albumin (BSA, Fisher BioReagents) in 0.01% Tween-20 for 2 h at room temperature. After washing 3 times in PBS, slices were incubated with COL type I primary antibody (1:50) (Invitrogen) in 1% PBS/BSA overnight at 4°C. The next day, slices were washed 3 times with PBS to get rid of the non-bonded molecules and incubated with 1:200 and anti-rabbit Alexa Fluor 647 (ThermoFisher) in PBS for 2 h at 4°C. The slices were then washed with PBS, and prepared for the HA immunostaining. For this, the slices were again blocked with 1% BSA in 0.01% Tween-20 for 2 h at room temperature and washed with PBS, thoroughly. Then, slices were incubated with HABP, biotinylated (1:100, Sigma-Aldrich) in 1% PBS/BSA overnight at 4°C. The following day, slices were washed 3 times in PBS and incubated with 1:200 FITC-Streptavidin (ThermoFisher) in PBS for 2 h at room temperature. The final sample observation was performed with the confocal microscope (Axio Observer Z1 LSM 800, Zeiss).

4.3. Cell experiments

4.3.1. Cell culture maintenance

Human sw480s colon adenocarcinoma cells were cultured in DMEM (Gibco, Sigma-Aldrich) supplemented with 10% Fetal Bovine Serum (FBS, Sigma Aldrich), 1% Glutamax (Gibco, Life technologies), and 1% Penstrip (Gibco, Life technologies). 20.000 cells/cm^2 cells were cultured in T-75 flasks, maintained at 37°, 5% CO2 humidified atmosphere, and harvested with 0.25% trypsin before seeding or passaging.

4.3.2. Seeding process

Cell seeding was performed in both slices and scaffold-based electrodes for electrical measurements and they were fully hydrated for 2 h and sterilized with 70% ethanol for an hour. Then, they were thoroughly washed with UHP water and PBS and left in cell media for 2 h at 37°C, to allow for protein adhesion. Slices were then seeded with 10 μL of 4×10^4 cell suspension and scaffold-based electrodes were seeded with 20 μL of 2.5×10^5 cell suspension on top of each sample and left incubating for 2 h at 37°C. Then, 400 μL and 800 μL of media were added to slices and scaffold-based electrodes, respectively, and kept incubating at 37°C, 5% CO_2. The media was changed every 3 days.

To validate the system, the anti-proliferative drug morin was added after 7 days of incubation. 1 μL of morin was added to cell culture media at day 7 at a concentration of 250 μM and left to actuate for a day to induce apoptosis of cells. Controls were treated equally.

4.3.3. XTT assay

Assessment of cell viability and proliferation of sw480 cells was performed using the XTT Cell Viability Assay Kit (Cell Signalling Technology Inc.) which consists of an indirect quantitative colorimetric assay detecting the cellular metabolic activities. In brief, 4×10^4 sw480s seeded on slices were cultured for 7 days. Culture media was replaced with 500 μL fresh media and 100 μl yellow tetrazolium salt XTT solution was added to each well. This reagent undergoes reduction into a highly colored formazan dye by dehydrogenase enzymes in metabolically active cells, enabling the estimation of live cells within a given cell culture. After 3.5 h incubation at 37 °C, 100 μl sample was collected from each well containing scaffold slices and transferred to a 96-well plate, followed by absorbance reading at 450 nm using a microplate reader TECAN SPARK®.

4.3.4. sw480s immunostaining

Sw480s were fixed in 4% paraformaldehyde (PFA, Thermofisher Scientific) for 20 min, at room temperature. All samples were thoroughly washed with PBS, permeabilized in 0.1% Triton x-100 for 15 min, and then blocked for nonspecific binding with 1% BSA and 0.1% Tween-20 for 1 h at room temperature. To label, the samples for nuclei and F-actin cytoskeleton, DAPI and Alexa Fluor 647 Phalloidin were used, respectively. Fluorescence images of cells within the scaffold were taken using an epifluorescence/confocal microscope (Axio Observer Z1 LSM 800, Zeiss).

4.3.5. Electrical monitoring of sw480s growth and apoptotic induction with morin

The impedance measurements were taken with a similar setup explained in section 4.2.1.3 under a laminar hood cabinet to ensure sterility and using cell culture media as the electrolyte. The analysis of the impedance data was performed using the NOVA software using the model described in Fig. 5 and SI. For the calculation of the pseudo-capacitance associated with a CPE in the R/Q branch, the following formula was used [33]:

Equation 2 $C = \frac{(RQ)^{\frac{1}{a}}}{R}$

where, Q is the magnitude of the CPE and a is the exponent of the CPE.

4.3.6. sw480s 2D microscopy, SEM and immunostaining characterization of morin antiproliferative treatment on sw480s

2D microscopy images of cells before and after morin treatment were taken with an Invitrogen EVOS XL core (Thermofisher, UK) digital inverted microscope.

Scaffold microstructure with cells before and after morin treatment was characterized using SEM (Leo Variable pressure SEM, ZEIS GmbH). In particular, SEM was used to visualize the presence of cells invading the scaffold before and after morin treatment. Briefly, cells in the scaffold were fixed in 4% PFA for 20 min at room temperature, washed thoroughly with PBS, dehydrated in graded ethanol series (50%, 75%, 95%, and 100% ethanol in water), and then in hexamethyldisilazane solution (Sigma Aldrich) until complete dehydration. Dehydrated samples were mounted on conductive carbon adhesive and analyzed at 1 kV power.

The changes in the nuclear morphology of sw480s on treatment with morin (250 μM) after 24 h were examined using the cell-permeable DNA dye, Hoechst 33342. After incubation, living cells were stained with Hoechst (2 μM) for 30 min at 37°C, followed by washing with PBS 3 times, and the nuclei were observed under a fluorescence microscope (Axio Observer Z1 LSM 800, Zeiss).

Cell apoptosis was measured using AnnexinV-fluorescein isothiocyanate (FITC)/PI staining. Briefly, cells were incubated on 250 μM morin for 24 h. Scaffolds were stained with a mixture of FITC-Annexin-V (5 μL) and PI (5 μL) in binding buffer (1000 μL), from the Annexin-V apoptosis detection kit (BD Biosciences) and incubated for 30 min at room temperature in the dark. Scaffolds were thoroughly washed with PBS and confocal images were taken within 1 h.

CRediT autorship contribution statement

Janire Saez: Conceptualization, Methodology, Formal analysis, Investigation, Writing – original draft, Writing – review & editing, Visualization, Funding acquisition. **Antonio Dominguez-Alfaro**: Conceptualization, Methodology, Investigation, Writing-review & editing. **Chiara Barberio**: Methodology, Writing – review & editing. **Aimee Withers**: Methodology, Writing – review & editing. **David Mecerreyes**: Supervision, Funding adquisition, Writing-review & editing. **Róisín M. Owens**: Supervision, Funding adquisition, Writing – review & editing.

Data availability statement

The data that support the findings of this study are available from the corresponding author upon reasonable request.

Declaration of competing interest

The authors declare that they have no known competing financial interests or personal relationships that could have appeared to influence the work reported in this paper.

Acknowledgments

This project has received funding from the European Union's Horizon 2020 research and innovation programme under the Marie Skłodowska-Curie grant agreement No. 842356 ICE-METs project. DM acknowledges the economic support of Spanish MCIN/AEI/PID2020-119026 GB-I00 and by Marie Sklodowska-Curie Research and Innovation Staff Exchanges (RISE) under the grant agreement No 823989 "IONBIKE".

Appendix A. Supplementary data

Supplementary data to this article can be found online at https://doi.org/10.1016/j.mtchem.2022.100990.

References

[1] H. Sung, J. Ferlay, R.L. Siegel, M. Laversanne, I. Soerjomataram, A. Jemal, F. Bray, CA A Cancer J. Clin. 71 (2018) 209–249.
[2] G. Carioli, M. Malvezzi, P. Bertuccio, P. Boffetta, F. Levi, C. La Vecchia, E. Negri, Ann. Oncol. 32 (4) (2021) 478–487.
[3] P.C. Benias, R.G. Wells, B. Sackey-Aboagye, H. Klavan, J. Reidy, D. Buonocore, M. Miranda, S. Kornacki, M. Wayne, D.L. Carr-Locke, N.D. Theise, Sci. Rep. 8 (2018) 4947.
[4] G. Jensen, C. Morrill, Y. Huang, Acta Pharm. Sin. B 8 (2018) 756–766.
[5] R. Edmondson, J.J. Broglie, A.F. Adcock, L. Yang, Assay Drug Dev. Technol. 12 (2018) 207–218.
[6] N. Chaicharoenaudomrung, P. Kunhorm, P. Noisa, J. World, Stem Cell. 11 (2019) 1065–1083.
[7] G. Lutzweiler, A. Ndreu Halili, N. Engin Vrana, Pharmaceutics 12 (2020) 602.
[8] S.T. Kreger, S.L. Voytik-Harbin, Matrix Biol. 28 (2009) 336–346.
[9] E.A. Turley, Cancer Metastasis Rev. 11 (1992) 21–30.
[10] B.S. Kubens, K.S. Zänker, Cancer Lett. 131 (1998) 55–64.
[11] A.G. Guex, J.L. Puetzer, A. Armgarth, E. Littmann, E. Stavrinidou, E.P. Giannelis, G.G. Malliaras, M.M. Stevens, Acta Biomater. 62 (2017) 91–101.
[12] M.N. Gueye, A. Carella, J. Faure-Vincent, R. Demadrille, J. Simonato, Prog. Mater. Sci. 108 (2020) 100616.
[13] I.M. Basurto, M.T. Mora, G.M. Gardner, G.J. Christ, S.R. Caliari, Biomater. Sci. 9 (2021) 4040–4053.
[14] Z. Daraeinejad, I. Shabani, Synth. Met. 271 (2021) 116642.
[15] N. Alegret, A. Dominguez-Alfaro, D. Mecerreyes, Biomacromolecules 20 (2019) 73–89.
[16] D. Mantione, I. Del Agua, A. Sanchez-Sanchez, D. Mecerreyes, Polymers 9 (2017) 354.
[17] A.I. Hofmann, D. Katsigiannopoulos, M. Mumtaz, I. Petsagkourakis, G. Pecastaings, G. Fleury, C. Schatz, E. Pavlopoulou, C. Brochon, G. Hadziioannou, E. Cloutet, Macromolecules 50 (2017) 1959–1969.
[18] A.R. Harris, P.J. Molino, A.G. Paolini, G.G. Wallace, Synth. Met. 222 (2016) 338–343.
[19] D.G. Harman, R. Gorkin, L. Stevens, B. Thompson, K. Wagner, B. Weng, J.H.Y. Chung, M. in het Panhuis, G.G. Wallace, Acta Biomater. 14 (2015) 33–42.
[20] I. del Agua, S. Marina, C. Pitsalidis, D. Mantione, M. Ferro, D. Iandolo, A. Sanchez-Sanchez, G.G. Malliaras, R.M. Owens, D. Mecerreyes, ACS Omega 3 (2018) 7424–7431.
[21] Y. Xu, P.A. Patsis, S. Hauser, D. Voigt, R. Rothe, M. Günther, M. Cui, X. Yang, R. Wieduwild, K. Eckert, C. Neinhuis, T.F. Akbar, I.R. Minev, J. Pietzsch, Y. Zhang, Adv. Sci. 6 (2019) 1802077.
[22] B. Yang, F. Yao, L. Ye, T. Hao, Y. Zhang, L. Zhang, D. Dong, W. Fang, Y. Wang, X. Zhang, C. Wang, J. Li, Biomater. Sci. 8 (2020) 3173–3185.
[23] D. Mantione, I. del Agua, W. Schaafsma, J. Diez-Garcia, B. Castro, H. Sardon, D. Mecerreyes, Macromol. Biosci. 16 (2016) 1227–1238.
[24] S. Inal, A. Hama, M. Ferro, C. Pitsalidis, J. Oziat, D. Iandolo, A. Pappa, M. Hadida, M. Huerta, D. Marchat, P. Mailley, R.M. Owens, Adv. Biosys. 1 (2017) 1700052.
[25] D. Iandolo, J. Sheard, G. Karavitas Levy, C. Pitsalidis, E. Tan, A. Dennis, J. Kim, A.E. Markaki, D. Widera, R. ó M. Owens, MRS Comm 10 (2020) 179–187.
[26] K. Thakur, Y. Zhu, J. Feng, J. Zhang, F. Hu, C. Prasad, Z. Wei, Food Funct. 11 (2020) 8424–8443.
[27] U. Lang, N. Naujoks, J. Dual, *Synth. Met.* 159 (2009) 473–479.
[28] D. Iandolo, F.A. Pennacchio, V. Mollo, D. Rossi, D. Dannhauser, B. Cui, R.M. Owens, F. Santoro, Adv. Biosys. 3 (2019) e1800103.
[29] J. Zhang, E. Wehrle, P. Adamek, G.R. Paul, X. Qin, M. Rubert, R. Müller, Acta Biomater. 114 (2020) 307–322.
[30] M. Hesam Mahmoudinezhad, A. Karkhaneh, K. Jadidi, J. Biosci. 43 (2018) 307–319.
[31] C. Pitsalidis, M.P. Ferro, D. Iandolo, L. Tzounis, S. Inal, R.M. Owens, Sci. Adv. 4 (2018) eaat425.
[32] T. Sithara, K.B. Arun, H.P. Syama, T.R. Reshmitha, P. Nisha, Front. Pharmacol. 8 (2017) 640.
[33] C. Moysidou, C. Pitsalidis, M. Al-Sharabi, A.M. Withers, J.A. Zeitler, R.M. Owens, Adv. Biology. 5 (2021) 2000306.